

Creative Commons Attribution 4.0 International (CC BY 4.0)

<https://creativecommons.org/licenses/by/4.0/>

Access to this work was provided by the University of Maryland, Baltimore County (UMBC) ScholarWorks@UMBC digital repository on the Maryland Shared Open Access (MD-SOAR) platform.

Please provide feedback

Please support the ScholarWorks@UMBC repository by emailing scholarworks-group@umbc.edu and telling us what having access to this work means to you and why it's important to you. Thank you.



Article

On the Sensitivity of a Ground-Based Tropospheric Lidar to Aitken Mode Particles in the Upper Troposphere

Matheus T. Silva ¹, Juan Luis Guerrero-Rascado ^{2,3}, Alexandre L. Correia ¹, Diego A. Gouveia ⁴
and Henrique M. J. Barbosa ^{1,5,*}

¹ Physics Institute, University of Sao Paulo, Sao Paulo 05508-090, Brazil

² Department of Applied Physics, University of Granada, 18071 Granada, Spain

³ Andalusian Institute for Earth System Research (IISTA-CEAMA), 18006 Granada, Spain

⁴ Royal Netherlands Meteorological Institute (KNMI), 3731 GA De Bilt, The Netherlands

⁵ Department of Physics, University of Maryland Baltimore County, Baltimore, MD 21246, USA

* Correspondence: hbarbosa@umbc.edu; Tel.: +1-(410)-455-1248

Abstract: Airborne observations have shown high concentrations of ultrafine aerosols in the Amazon upper troposphere (UT), which are key for replenishing the planetary boundary layer (PBL) with cloud condensation nuclei that sustain the “green ocean” clouds. Given their climatic relevance, long-term observations are needed, but aircraft measurements are only available in short-term campaigns. Alternatively, continuous observations of the aerosol vertical structure could be performed by a lidar (acronym for “light detection and ranging”) system in long-term campaigns. Here we assess whether a ground-based tropospheric lidar system could detect these ultrafine UT aerosols. To this aim, we simulated the lidar signal of a real instrument and then varied the instrument’s efficiency and the UT-particle concentration to determine under which conditions the detection is possible. Optical properties were computed with a Mie code based on the size distributions and numerical concentration profiles measured by the aircraft, and on the refractive indexes inverted from AERONET measurements. The aerosol optical depth (AOD) was retrieved by inverting the elastic lidar signal, and a statistical test was applied to evaluate the detection of the UT-aerosol layer. Our results indicate that, for the instrument we simulated, a 55-fold increase in the signal-to-noise ratio (SNR) is required for a 100% detection rate. This could be achieved by simultaneously time averaging over 30 min and spatially averaging to vertical bin lengths of 375 m, or by modifying the hardware. We repeated the analysis for under- and overestimated aerosol lidar ratio (L_{aer}), and found that possible systematic errors did not affect the detection rate. Further studies are necessary to assess whether such long-time averages are feasible in the Amazon region (given the very high cloud cover), and to design a hardware upgrade. Although simulations and analyses here were based on a particular instrument and for the presence of new organic particles in the Amazonian upper troposphere, our methodology and results are general and applicable to other instruments and sites.

Keywords: elastic lidar; sensitivity; signal-to-noise ratio; Monte Carlo simulation; Amazon; new particle formation



Citation: Silva, M.T.; Guerrero-Rascado, J.L.; Correia, A.L.; Gouveia, D.A.; Barbosa, H.M.J. On the Sensitivity of a Ground-Based Tropospheric Lidar to Aitken Mode Particles in the Upper Troposphere. *Remote Sens.* **2022**, *14*, 4913. <https://doi.org/10.3390/rs14194913>

Academic Editor: Simone Lolli

Received: 28 July 2022

Accepted: 28 September 2022

Published: 1 October 2022

Publisher’s Note: MDPI stays neutral with regard to jurisdictional claims in published maps and institutional affiliations.



Copyright: © 2022 by the authors. Licensee MDPI, Basel, Switzerland. This article is an open access article distributed under the terms and conditions of the Creative Commons Attribution (CC BY) license (<https://creativecommons.org/licenses/by/4.0/>).

1. Introduction

In the context of climate change, the Amazon rainforest plays a crucial role in the global hydrological, biogeochemical and energy cycles [1–3]. The region has approximately 5 million square kilometers of preserved forest, and is the world’s largest terrestrial carbon reservoir [4]. There is intense evapotranspiration, and clouds are omnipresent even during the dry season. Several studies highlight the importance of water vapor recycling [5] and transport, carrying humidity to other regions [6,7]. Nonetheless, anthropogenic changes are already disturbing the natural functioning of the forest [8,9]. Biomass burning in the Arc of Deforestation emits aerosol particles that cover the entire region [10,11] and reach

all over South America [12]. Even in pristine parts of the forest, aerosol particle number concentration increases by 10-fold in the dry season (from about 220 to 2200 cm⁻³), and so does aerosol optical depth (AOD) at 550 nm (from 0.1 to about 1.0) [10]. Interactions between deforestation, fire and climate change are likely to further alter carbon storage [13], moisture transport [14,15] and precipitation patterns [16]. In turn, such changes in the Amazon basin atmosphere are expected to affect the global climate [17–19].

In pristine conditions, cloud formation in the Amazon depends exclusively on the few secondary organic aerosol (SOA) particles acting as cloud condensation nuclei (CCN) (concentrations of about 150–300 cm⁻³ during the wet season, e.g., [20]). These particles are formed by biogenic volatile organic compound (BVOC) precursors, but their nucleation is rarely observed by ground measurements [21–24]. Recently, a conceptual model that explains the life cycle of SOAs in the Amazon atmosphere was proposed, suggesting that new SOA particles are nucleated in the upper troposphere (UT) from BVOCs transported by cloud updrafts [25,26]. These new aerosol particles are transported into the planetary boundary layer (PBL) by downward mixing, sustaining the CCN population that feeds the green ocean clouds. However, the current knowledge of this mechanism must be improved in order to allow its representation in global climate models [27]. This conceptual model was based on observations from aircraft measurements during GoAmazon2014/5 [28] and ACRIDICON-CHUVA [29] campaigns. However, aircraft campaigns are expensive and sporadic, and hence cannot provide the long-term measurements needed to further our understanding of the aerosol life-cycle. Ground-based remote sensing techniques, particularly aerosol lidar, could help to fill this gap.

The first reported long-term lidar measurements of aerosol profiles in the Amazon were conducted in the framework of EUCAARI and AMAZE-08 projects in 2008 [30–32]. The authors showed the presence of African smoke and dust on 32% of all profiles analyzed during the wet season, with a maximum smoke AOD contribution of 0.15 at 532 nm in February of that year. In a follow-up study, the same group reported intrusions of Saharan dust [11]. Using airborne lidar observations, Marenco et al. [33] reported that the UK Unified Model and the ECMWF-MACC model generally reproduced the observed vertical distribution of biomass-burning aerosols. However, the authors highlighted that both models tended to fail close to individual fires or in the vicinity of clouds. Barbosa et al. [34] discussed the performance of a lidar instrument operating in the Amazon region. They presented a validation analysis comparing the AOD from lidar measurements with those from AERONET (Aerosol RObotic NETwork [35]), finding a root-mean-squared error of about 0.06. None of these early studies investigated the presence of aerosols in the Amazon's upper troposphere.

Our main goal here was to statistically evaluate whether a ground-based lidar system could detect ultrafine particles in the Amazon UT layer (between 9 and 15 km). We developed a simulation of the lidar signal based on aerosol physical in situ measurement from recent aircraft campaigns, and from aerosol optical properties from AERONET. The simulation had the same efficiency and hence mimicked the experimental lidar signal. The methodology is described in detail in Section 2. Using the Monte Carlo approach mentioned in Section 2.3, we performed thousands of simulations varying the aerosol concentration and lidar efficiency to find conditions that allow for the detection of the thin layer of ultrafine particles, despite the typical noise in lidar signals at UT altitudes. The results are presented and discussed in Sections 3 and 4. Our recommendations for improving the detection efficiency and conclusions are presented in Section 5.

2. Materials and Methods

2.1. Lidar LFA IF-USP

The observation data used for calibrating the simulations were measured by the LFA IF-USP lidar, which was operated at the Manaus_EMBRAPA site (2.89°S, 59.97°W) from 2011 to 2017, with a co-located AERONET station. The instrument uses a Quantel CFR-400 Nd-YAG laser with 95 mJ per pulse at 355 nm and 10 Hz repetition rate. The receiver

subsystem has a telescope area of 0.13 m², and filters in the 355 nm (elastic), 387 (N₂) and 408 (H₂O) nm bands. The transient recorder operates at 20 MHz. The acquisition interval is typically configured for 30 s or 1 min. More details about the instrument are given by Barbosa et al. [34]. In this study, we simulated the 355 nm elastic signal in photon-counting mode. In this mode, the acquisition hardware counts the individual photons arriving at the photo-multiplier tube (PMT), and hence the signal follows a Poisson probability function [36]. To avoid the saturation of the photon-counting at lower altitudes, we glued the analog and photon-counting signals [37]. The data used as a reference in this study had a raw time resolution of 30 s and a raw vertical resolution of 7.5 m.

2.2. Lidar Signal Simulation

The lidar equation describing the number of elastic photons with wavelength λ detected as a function of the altitude z can be written as:

$$P(z, \lambda) = \frac{E_0}{E_{phot}} dz A \eta \frac{O(z)}{z^2} \beta(z, \lambda) \exp\left(-2 \int_0^z \alpha(z', \lambda) dz'\right) \quad (1)$$

where E_0 , E_{phot} , dz , A , η e $O(z)$ are the energy per laser pulse, energy per photon, vertical bin length, telescope area, overall system efficiency and overlap function, respectively. β and α are the backscattering and extinction coefficients, respectively, which account for the extrinsic optical properties of aerosols and molecules as indicated below:

$$\beta(z, \lambda) = \beta_{mol}(z, \lambda) + \beta_{aer}(z, \lambda) \quad (2)$$

$$\alpha(z, \lambda) = \alpha_{mol}(z, \lambda) + \alpha_{aer}(z, \lambda) \quad (3)$$

where the subscripts “mol” and “aer” respectively stand for molecules and aerosols. For air molecules, the optical properties were simulated based on Bucholtz [38] and Bodhaine et al. [39], using the standard tropical profile of pressure and temperature [40].

For the aerosol optical properties, Mie calculations were performed using the radiative transfer package libRadtran [41]. The number size distribution of ultrafine particles was based on GoAmazon 2014/5 campaign measurements aboard the G-1 aircraft [28], which are shown in Figure 9 of Andreae et al. [25]. The authors report measurements up to 5800 m, close to the maximum flying altitude of the aircraft. Because the distributions at 4500 and 5800 m have approximately the same median radius and standard deviation for their Aitken modes, we assumed those to be representative of the Aitken mode in the UT layer. Close to the surface, the size distribution measured by the aircraft shows an accumulation mode only. This is due to the size cut-off of the instrument, which could not measure larger particles. For this reason, we analyzed the volume size distribution from the AERONET inversion products to obtain the median radius and standard deviation of the fine and coarse mode aerosols, which we assumed to be representative of the aerosols in the PBL. We used data from the Manaus_EMBRAPA site and averaged all 764 size distributions obtained from 8 years (2011–2019) of level 1.5 measurements during the dry season (Jul–Nov).

For the real (\Re) and imaginary (\Im) refractive indexes, we considered those reported by the same AERONET station at 440 nm. Values retrieved with $AOD_{440} < 0.4$ were excluded from the analysis, as suggested by Holben et al. [42]. Since no significant differences were observed between refractive indexes in the dry (Jul–Nov) and wet (Dec–Jun) seasons, data from both seasons were combined and the same refractive indexes were used to simulate the UT and PBL aerosol optical properties. Table 1 lists the parameters used for particles in the UT and at the PBL. Note that the UT’s refractive indexes and L_{aer} were randomized in the Monte Carlo experiments discussed further below, while the values in the PBL were kept fixed.

The aerosol lidar ratio L_{aer} and extinction-to-mass coefficient α_{aer}^{mass} were obtained by Mie calculations. The extinction-to-mass coefficient has units of m^{−1} (g/m³)^{−1}, and was multiplied by the profile of aerosol mass concentration (in g/m³) to obtain the extinction

coefficient α_{aer} in m^{-1} . The backscatter coefficient, β_{aer} , in $\text{m}^{-1} \text{sr}^{-1}$ was determined by the quotient of α_{aer} and L_{aer} .

Table 1. Properties of aerosols in the upper troposphere (Aitken mode) and the boundary layer (fine and coarse modes) used as input to the Mie code and lidar signal simulations. Number size distributions are log-normal with median radius R_g and geometric standard deviation σ_g . Real (\Re) and imaginary (\Im) refractive indexes were obtained from 8 years of AERONET measurements at the Manaus_Embrapa site. The aerosol lidar ratio L_{aer} is calculated by the Mie code and varies with the refractive index. The altitude range and concentration are based on the median profile shown by Andreae et al. [25], which was approximated by two aerosol layers as shown in Figure 1. Ranges in brackets, corresponding to the 10th and 90th percentiles, are given for the parameters randomized in the Monte Carlo experiments. Number, mass, extinction and AOD of the UT aerosol layer were varied in the sensitivity experiments, from $1\times$ to $16\times$ the values shown here.

Parameters	Upper Troposphere	Planetary Boundary Layer
R_g (nm)	23	85 and 236
σ_g	1.6	1.5 and 2.4
\Re (440 nm)	[1.40 to 1.56]	1.46
\Im (440 nm)	[0.00052 to 0.00944]	0.0021
L_{aer} (sr)	[20.2 to 23.5]	60.3
Layer Top (km)	15	2
Layer Base (km)	9	0
Number Conc. (cm^{-3})	$N_{0,ut} = 1246$	$N_{0,pbl} = 1251$ and 4.9
Mass Conc. ($\mu\text{g m}^{-3}$)	0.25	11.2 and 16.0
Extinction (Mm^{-1})	0.37	88.4
AOD	0.0022	0.18

The mass concentration was obtained from the number concentration and the normalized log-normal size distributions for each aerosol log-normal mode, assuming an aerosol density of 1.5 g cm^{-3} . The number concentration was taken from the median of all aircraft measurements, as shown in Figures 7a and 10a of Andreae et al. [25]. The Aitken mode concentration was the ultrafine fraction ($<90 \text{ nm}$) of the total concentration, while that in the boundary layer was the non-ultrafine fraction. For our simulations, we considered a simplified profile with two aerosol layers (see Figure 1). The UT layer had a uniform number concentration between 9 and 15 km with Aitken mode aerosol, while the boundary layer aerosols had fine and coarse modes with constant concentrations from the surface to 2 km. The values used in the simulations are given in Table 1. $N_{0,ut}$ and $N_{0,pbl}$ were calculated as the layer mean value of the observed concentration of Amazon upper-troposphere and planetary boundary layer particles, respectively. The concentration was assumed to be zero outside these two layers. For the sensitivity experiments, we increased the value of $N_{0,ut}$, as explained in the next sections.

Finally, the performance parameters of Equation (1) were set based on the LFA IF-USP lidar. Energy per laser pulse was $E_0 = 95 \text{ mJ}$, telescope area was 0.13 m^2 and vertical resolution was $dz = 7.5 \text{ m}$. The incomplete overlap between the telescope field of view and the laser beam was not included in the simulation, because the same overlap would be used for performing the inversion of the signal. The efficiency η was estimated by calibrating the simulated signal, i.e., by a molecular fit on a 1 h mean profile (21:00 to 22:00 h LT) of the LFA IF-USP lidar measurements between 16 and 26 km. Figure 2 shows the range-corrected lidar signal for a single 30 s profile in blue and the molecular reference in black. From the molecular calibration, we obtained an efficiency of 0.75%. This is an estimation of the overall efficiency in the system, which includes optical (e.g., filters and lenses) and detection efficiencies (e.g., photocathode quantum efficiency).

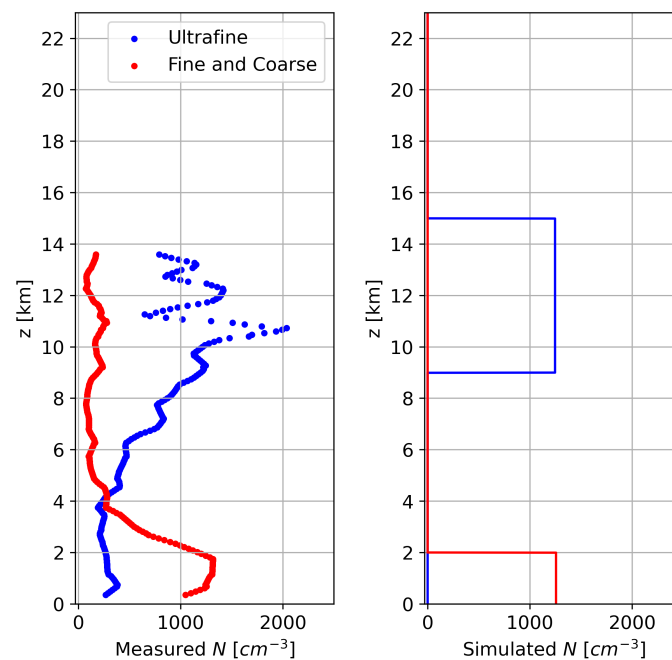


Figure 1. Median aerosol number concentrations measured by the HALO aircraft (left) and the 2-layer representation adopted in our simulations (right), for the ultrafine (blue) and fine plus coarse particles (red). The values shown are not corrected for standard temperature (273.15 K) and pressure (1000 hPa).

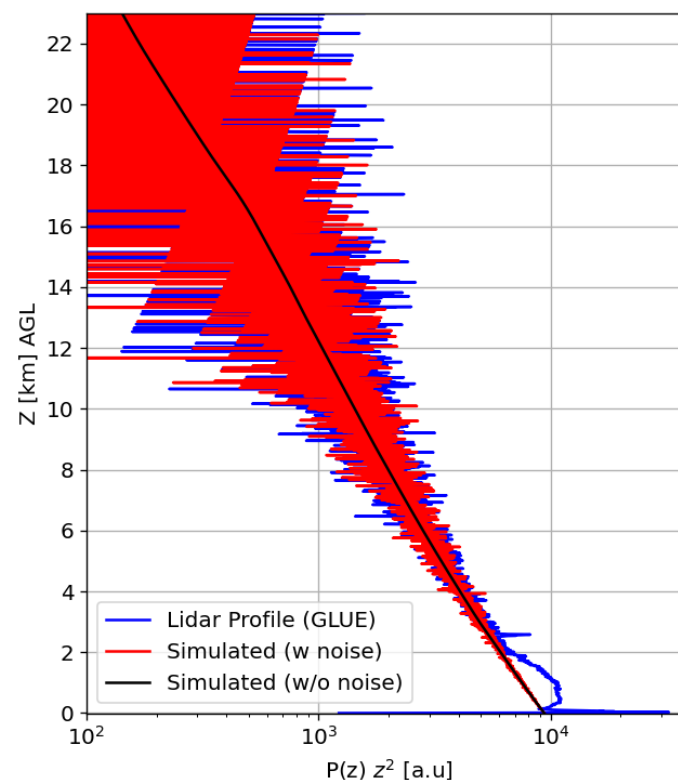


Figure 2. Vertical profiles of the range-corrected lidar signals are shown for a single 30 s measurement at 21:00 h LT on 14 September 2014 (blue), the simulated molecular signal with noise (red) and the molecular reference without noise (black). The reference was calibrated from 16 to 26 km using the average of all 30 s measurements from 21:00 to 22:00 h LT. The measured photon-counting and analog signals were glued and corrected for the instrument overlap. The signal shows aerosols in the PBL below 2 km.

The comparison between the measured and simulated signals shows excellent agreement for both the mean value and the Poisson noise. This example is for 14 September 2014, when AERONET reported an atmosphere with AOD of about 0.4, mostly due to particles in the PBL, below 2 km.

2.3. Detection Algorithm

For a 30 s backscatter profile, as in the example in Figure 2, the signal-to-noise ratio at the base (top) of the UT layer was very low, around 4.6 (1.7) and precluded detection of the signal of the ultrafine aerosol particles. To understand under which conditions such detection would be possible, we varied the system efficiency and the aerosol concentration in our simulations.

In this study, Klett–Fernald inversion algorithm [43,44] was applied, assuming the known average L_{aer} to retrieve $\beta(z)$ and $\alpha(z)$, from which the AOD in the UT layer, AOD_{UT} , was calculated. Uncertainties in these aerosol optical properties were calculated using a Monte Carlo approach, where the lidar signal was resampled 100 times by drawing from the Poisson distribution of the measured signal. To avoid the need to visually inspect the optical profiles for the presence of aerosols in the UT, a quantitative detection algorithm was applied. The algorithm compares AOD_{UT} with its uncertainty and computes the z-score as AOD_{UT}/σ_{AOD} . Aerosols were considered to be present in the UT when the $AOD_{UT} > 0$ with statistical significance at the 99.7% level, i.e., when z-score > 3 . Note that this detection method does not locate the top and bottom of the aerosol layer, it merely informs whether there is a significant AOD from 9 to 15 km, i.e., whether there are aerosols in the UT.

2.4. Sensitivity Experiments

Lidar signals were simulated for 5 different values of the system efficiency and 5 different values of the ultrafine aerosol concentrations in the UT layer ($N_{0,ut}$). The aerosol number concentration in the PBL ($N_{0,pbl}$) was kept fixed as 1256 cm^{-3} . Here, the efficiency (κ) and the ultrafine aerosol number concentration (ν) factors represent how much each quantity was increased compared to their reference values. κ was simulated for values of 1, 10, 100, 1000 and 10,000, where $\kappa = 1$ represents an LFA IF-USP lidar efficiency of 0.75%. Similarly, ν was simulated for the values of 1, 2, 4, 8 and 16, where $\nu = 1$ represents the aerosol number concentration ($N_{0,ut}$) of 1246 cm^{-3} at UT—the median value measured by the aircraft (Table 1).

This range of concentration values was used because there were flights which detected much greater values than the median. Andreae et al. [25] reported UT ultrafine concentrations ranging approximately between 2000 and $19,000 \text{ cm}^{-3}$ at standard temperature and pressure (STP: $T_0 = 273.15 \text{ K}$ and $p_0 = 1000 \text{ hPa}$), reaching up to $65,000 \text{ cm}^{-3}$ (STP) in some cases. On the other hand, the range of efficiency values was chosen to allow a definite detection for any number concentration chosen. Whether a large improvement in efficiency is feasible and how it could be achieved will be discussed later.

Altogether, there were 25 combinations of κ and ν , for which 100 lidar profiles were simulated in a Monte Carlo approach. Each repetition represents one “experiment” with the same κ and ν , but with different Poisson noise and different aerosol optical properties, drawing from our database of AERONET’s index of refraction. For each experiment, the detection algorithm described in the previous section was applied. The frequency of detection f was calculated as the ratio between the number of successful detections and the total number of experiments. Note that we applied two Monte Carlo methods: one to obtain the uncertainties of the aerosol optical properties retrievals and another to obtain “ f ”. From all 25×100 simulations, maps of frequency of detection as a function of the system efficiency and ultrafine aerosol number concentration were built.

Differences between the L_{aer} used in the Klett–Fernald inversion (hereafter L_{aer}^{inv}) and the L_{aer} of the actual particles in the atmosphere can lead to systematic biases in the retrievals [34,45,46]. Because the L_{aer} has a natural variability, the best-case scenario for the analysis of a lidar signal is when the average L_{aer} in the atmosphere is known. Therefore,

to evaluate whether such a bias could affect our estimates of the detection efficiency, our simulations were repeated, and the inversions were performed using a range of L_{aer}^{inv} values above and below the mean value of L_{aer} . This was done only for the Aitken particles in the UT because using a biased lidar ratio for the boundary aerosols would not distort the retrieved extinction in the UT.

3. Results

Our goal was to perform a sensitivity analysis to evaluate whether a typical ground-based lidar for tropospheric aerosols could detect ultrafine particles in the Amazonian upper troposphere. The analysis scheme consisted of changing the aerosol number concentration in the UT layer and the instrument detection efficiency to values above our baseline. This baseline considers the median profile of the aerosol concentration reported by aircraft measurements and the typical signal-to-noise ratio of a single 30 s lidar profile.

Figure 3 shows the effect of increasing the instrument efficiency (κ) from 1 to 10,000, for a situation where $\nu = 16$. Hence, the concentration in the UT was $16\times$ that shown in Figure 1, which corresponds to an extinction of 6.0 Mm^{-1} and AOD of 0.035 in the UT layer. It should be noted that the noise in the UT was lower than in the troposphere because of the different L_{aer} used in the retrieval (22 and 60 sr, respectively). For $\kappa = 1$ (left panel), the noise in the retrieved extinction in the UT was significantly larger than the simulated extinction, hence the aerosol layer was not detectable. For the largest values ($\kappa = 1000$ and 10,000), the noise was reduced by a factor of $\sqrt{\kappa}$, and the aerosol layer was identifiable. For intermediate values ($\kappa = 10$ and 100), visual inspection was not sufficient and it was necessary to rely on the statistical detection method. The z-score is indicated in each panel and, for this example with $\nu = 16$, even a value of $\kappa = 10$ was sufficient for the detection of the layer ($z = \text{AOD}/\sigma_{\text{AOD}} = 5 > 3$).

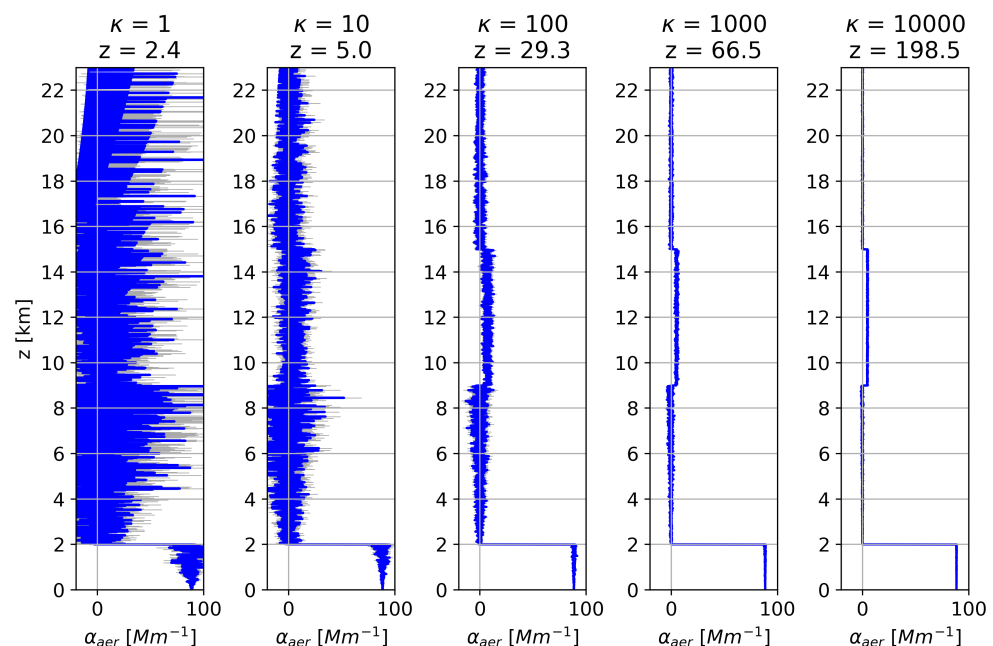


Figure 3. Example of extinction profiles obtained by the Klett–Fernald inversion of lidar signals simulated with κ varying from 1 to 10,000, and $\nu = 16$. Although the Monte Carlo method varies the simulated L_{aer} , here α_{aer} is held constant to allow a direct comparison between panels. The inversion used the exact average value of the L_{aer} at the UT (22 sr).

Figure 4 shows the same analysis but with the aerosol number concentration ν varying from 1 to 16. From the first to the last panel, the extinction noise and the horizontal axis scale are equal because they all correspond to the same efficiency of $\kappa = 10,000$. The situation was similar to that previously discussed. The aerosol layer was detectable for the two largest

number concentrations, and was undetectable for the lowest one. However, looking at the results of the statistical detection method, the retrieved AOD in the UT was statistically significant even when $\nu = 1$ ($z = 13.6 > 3$).

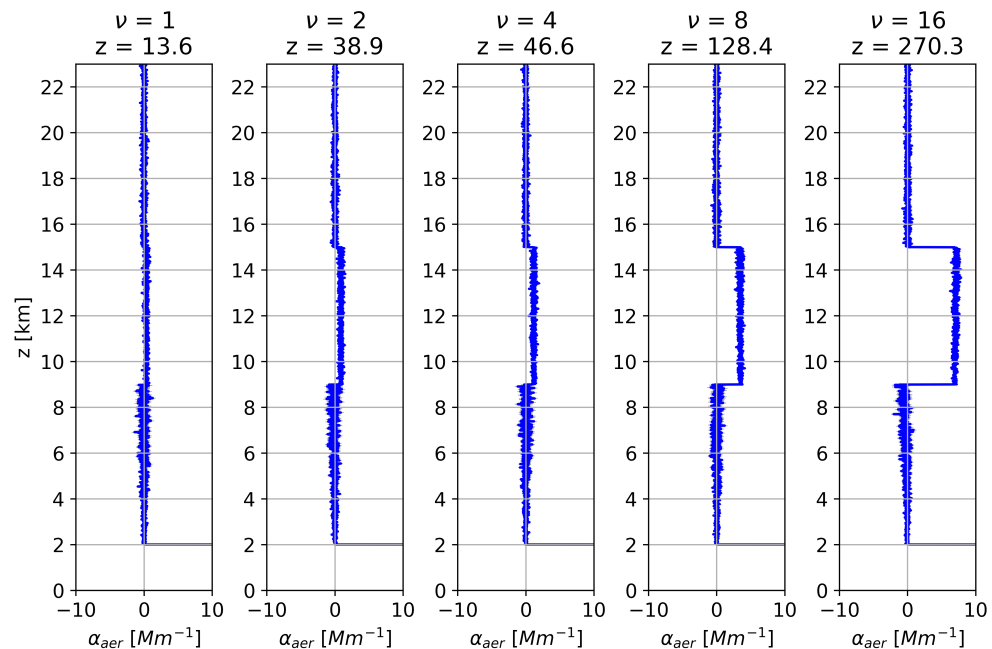


Figure 4. As Figure 3, but for ν varying from 1 to 16, and $\kappa = 10,000$. The x-scale is truncated at 10 Mm^{-1} to emphasize the UT.

As explained in Section 2.4, this analysis was repeated for each of the 25 combinations of κ and ν values, and we used a Monte Carlo approach to estimate the detection frequency. Figure 5 shows the result as a detection map. Values in dark red indicate the combinations of κ and ν where the detection was achieved in 100% of the Monte Carlo experiments, which occurred for large efficiency and/or large number concentrations. However, the larger the concentration, the less likely this situation was to occur in the actual atmosphere. The median number concentration measured by aircraft was $\nu = 1$, while $\nu = 16$ surpassed the 90th percentile. Considering the median as a reference ($\nu = 1$), the analysis indicates a guaranteed detection for an efficiency between 1000 and 10,000 times greater than the LFA IF-USP lidar (a signal-to-noise ratio 100 times greater).

The detection efficiency map was built under an ideal scenario. The lidar signals were simulated allowing the Aitken mode particles L_{aer} to vary around 22 sr as for a real atmosphere, but our analysis used the exact average value of that L_{aer} in the inversion to retrieve the optical properties, i.e., without any biases.

It is well-known that the solution of the elastic lidar equation derived by the Klett–Fernald method depends on the choice of lidar ratio, which affects the magnitude of both the extinction and backscatter profiles. Hence, a biased lidar ratio could in principle interfere with our methodology to detect the UT aerosol layer, because it is based on the AOD value. Therefore, it is important to evaluate the effects of underestimating or overestimating the L_{aer}^{inv} used in the inversion on the extinction retrievals and the detection frequency.

Figure 6 shows an example of retrieved extinction profiles above 2 km for fixed values of $\kappa = 10,000$ and $\nu = 16$ and a range of L_{aer}^{inv} values. The lidar signal was simulated with a refractive index of $1.52 + 0.005i$ at the UT layer, corresponding to an L_{aer} of 22 sr and an $AOD_{UT} = 0.041$. The title of each panel shows the aerosol L_{aer}^{inv} , where it was underestimated on the left, exact in the middle (with 22 sr) and overestimated on the right. The extinction increased with the L_{aer}^{inv} as expected, but so did its uncertainty. This effect is visible in the sequence of panels, and in the corresponding AOD_{UT} values reported in Table 2.

The AOD_{UT} bias was -32% for an underestimation of -9 sr (-40%), and was $+25\%$ for an overestimation of $+9$ sr ($+40\%$) of the L_{aer} .

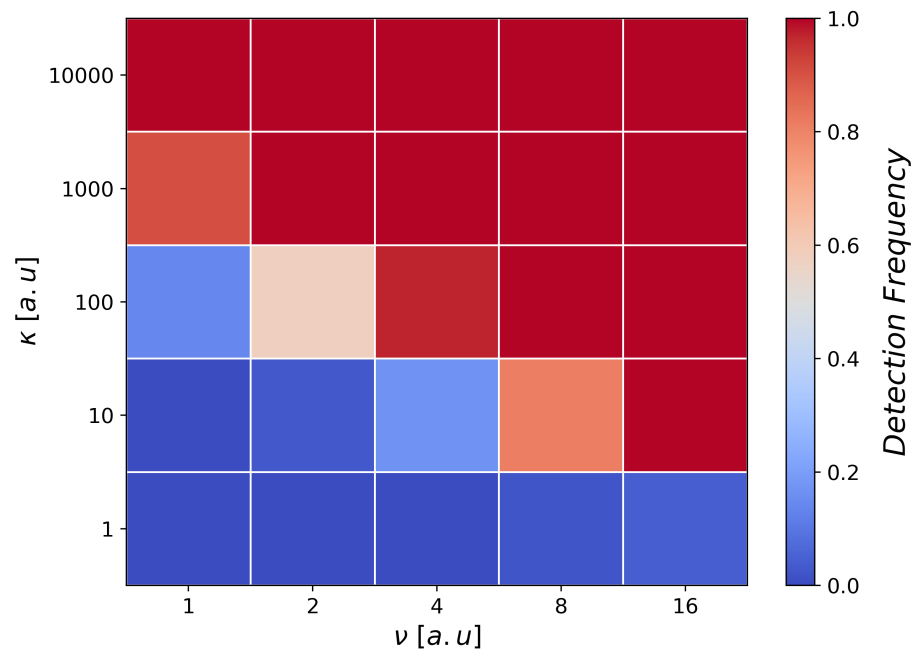


Figure 5. Detection map for the 25 combinations of κ and ν values, where colors represent the detection frequency (ranging from 0 to 1).

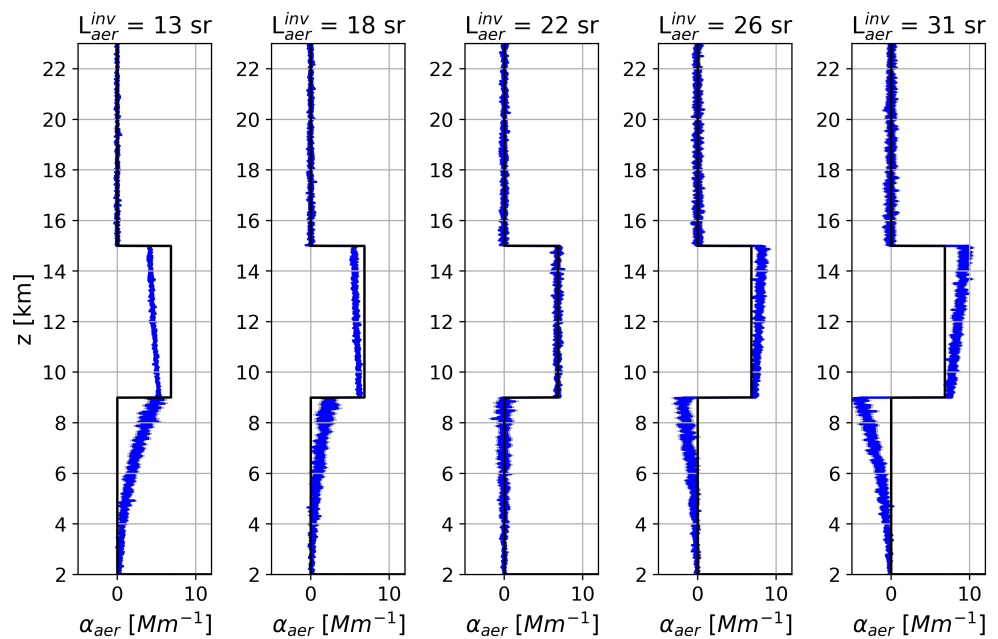


Figure 6. Examples of extinction profiles obtained with a range of values of L_{aer}^{inv} from 13 to 31 sr are shown in blue, with the reference value used in the simulation in black. The simulation was for the case of $\kappa = 10,000$ and $\nu = 16$.

This increase of the AOD_{UT} with the lidar ratio could affect the detection frequency. However, the uncertainty of AOD_{UT} also increased with the lidar ratio and, as shown in Table 2, there was little change in the z-score for the example in Figure 6. To understand how systematic errors in the L_{aer}^{inv} impacted the detection analysis, over the simulated range of κ and ν values, the detection maps were calculated for the five lidar ratios in Table 2.

Table 2. Retrieved AOD_{UT} and its uncertainty σ_{AOD} for each profile of Figure 6. L_{aer}^{inv} is the aerosol lidar ratio for ultrafine particles used in the inversion. The detection algorithm uses the z-score, which is the ratio AOD_{UT}/σ_{AOD} .

L_{aer}^{inv} (sr)	13	18	22	26	31
AOD_{UT}	0.02791	0.03495	0.04105	0.04629	0.05112
σ_{AOD}	0.00008	0.00010	0.00011	0.00013	0.00014
z-score	346	351	361	365	368
Bias AOD (%)	−32	−15	0	13	25
Bias σ (%)	−28	−12	0	14	23
Bias z-score (%)	−4.1	−2.8	0	1.1	1.9

Comparing the maps in Figure 7, no systematic disparities were clearly identified. Figure 8 supports this statement. Each line is a slice on the maps at $\nu = 1$, and includes additional simulations for 50 different levels of κ . Considering the uncertainties, none of the L_{aer}^{inv} values were significantly better for the detection of particles in the UT. This indicates that the effects of lidar ratio bias on the AOD_{UT} and on the AOD_{UT} uncertainty compensated each other. Therefore, the z-score did not vary significantly and the detection was not affected. Finally, it is also possible to note in Figure 8 that, with the larger number of κ values, the full detection (in 100% of the Monte Carlo experiments) occurred for a κ value of around 3000.

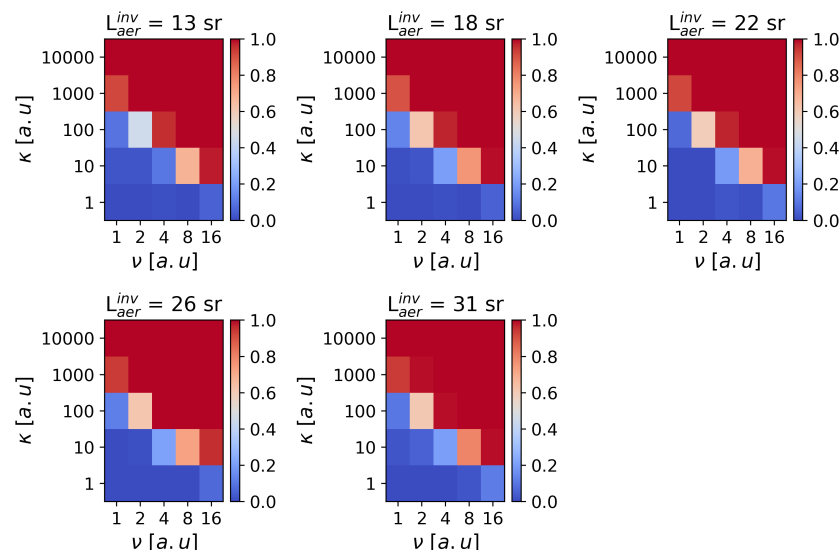


Figure 7. Maps of detection for the 25 combinations of κ and ν values, where the colors represent the detection frequency (ranging from 0 to 1). Each panel shows the biased inversion, with L_{aer}^{inv} varying from 13 to 31 sr.

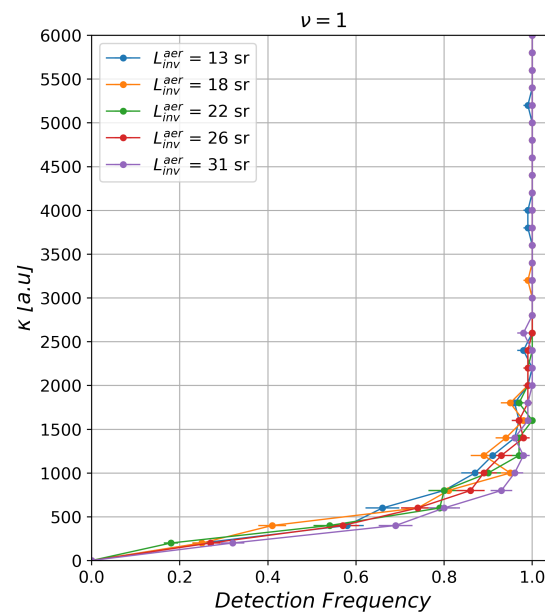


Figure 8. Detection frequency for $\nu = 1$ and κ varying from 1 to 6000 in steps of 200. Different colors indicate the L_{aer}^{inv} values used.

4. Discussion

The results above suggest that the detection of ultrafine particles in the Amazonian upper troposphere by the lidar technique is possible. For our reference system, the detection of the UT layer with the observed median concentration ($\nu = 1$) was guaranteed only if the system efficiency was improved by a factor of 3000, which is equivalent to an increase of the SNR by a factor of $\sqrt{3000} (\approx 55)$. These improvement factors were relative to the original SNR of our 30 s profiles. In absolute terms, the requirement for any lidar is to have an SNR of about 217 at 9 km and 80 at 15 km altitude. This condition is for the detection of the UT aerosol layer with the measured median number concentration and the Mie simulation of the optical properties. According to our calculations, this aerosol layer has an AOD at 355 nm of 0.0022 with a 23% uncertainty that is attributable to the variability of the refractive indexes.

This improvement could be achieved by combining a time average of 30 min (60 profiles of 30 s) and a vertical resolution of 375 m (50 bins of 7.5 m). Vertically averaging reduces our ability to differentiate very thin layers, but 375 m would still be sufficient to measure internal variations in the UT layer given that it extends over a height range of 6 km. On the other hand, finding long periods without clouds in the Amazon region can be very challenging [45]. A follow-up study would be necessary to investigate the frequency of low clouds, from the point of view of a nadir-looking narrow-beam instrument. An alternative to increasing the time and spatial averages would be to modify the hardware. Easy upgrades include removing the neutral density filter (currently has 50% of transmission) and doubling the laser power or shot frequency. These would give a factor of 4 in the number of photons detected, allowing us to lower the time average to about 15 min. Nonetheless, higher numbers of photons incident on the PMT could surpass its maximum range. To implement such improvements, an in-depth study of all optical components must be done.

For our instrument, the data acquisition works in both analog (AN) and photon-counting (PC) modes. The AN mode dynamical range is roughly 166 (12-bit ADC) and the PC dynamic range is about 300, which can be “glued” [47] to achieve a dynamic range of about 400 for 30 s profiles. This is about two orders of magnitude less than what is needed to simultaneously measure the aerosols in the boundary layer and the upper troposphere. From our simulations with the median aerosol number concentration in the UT, the difference in the signal from the PBL (800 m above the ground) to the aerosol-

free region above the UT layer (20 km above the ground) was estimated to be a factor of 30,000. To reach this dynamic range and the necessary SNR at the UT, the use of a long time-averaging will be unavoidable.

To our knowledge, similar studies evaluating the detection efficiency of thin aerosol layers as a function of the instrument efficiency and the aerosol number concentration have not yet been reported. For instance, Gouveia et al. [45] performed a similar analysis but for the detection of cirrus clouds in the Amazon. The authors also used a Monte Carlo approach to calculate the detection frequency, but they did this as a function of the SNR below the cloud and the cirrus backscatter coefficient. Moreover, instead of estimating the necessary increase in the system efficiency to detect the particles, they computed the minimum measurable cloud optical depth (COD) for their instrument efficiency.

Torres et al. [48] performed simulations of satellite-born lidar signals to study the aerosol radiative forcing above clouds, with a focus on the top of atmosphere (TOA) reflectance, which depends on the AOD above clouds and the COD. The authors estimated the error in the lidar-retrieved AOD and COD from possible systematic errors in the Ångström absorption exponent, single scattering albedo and aerosol–cloud separation. Another study, by Thorsen et al. [49], that computed the systematic error in AOD retrievals from lidar inspired the analysis developed here. The AOD error was obtained by lidar measurements on the Cloud-Aerosol Lidar and Infrared Pathfinder Satellite Observations [50,51] (CALIPSO) satellite sensor, underestimating the global average AOD [49]. The investigation separates two cases: “transparent”, when the laser completely passes through the layers of clouds and aerosols, and “without clouds”. For the first, a daytime underestimation bias of 54% was found, while for the second it was 47%. At night, the bias dropped to 38% and 22%, respectively. Although the authors found that a system capable of detecting a backscattering coefficient (at 532 nm) of $1\text{--}2\text{ km}^{-1}\text{ sr}^{-1}$ is required to reduce the bias to 1%, nothing about improving the SNR or the system efficiency was reported.

5. Conclusions

We studied the sensitivity of a ground-based tropospheric lidar operating in the near UV to the detection of ultrafine particles in the upper troposphere. By calculating the detection frequency as a function of the system efficiency and ultrafine aerosol concentration, we determined the conditions under which the detection was possible. For the median ultrafine aerosol concentration measured by aircraft campaigns in the Amazon, the detection was feasible for an SNR around 217 at 9 km and 80 at 15 km of altitude, corresponding to the base and top of the UT layer, respectively. In other words, an increase by a factor of about 55 in the SNR of the LFA IF-USP lidar would be necessary. While considering possible biases in the ultrafine particles lidar ratio L_{aer} , it was found that they would not affect these estimates. This is because the L_{aer} affects both the retrieved optical depth and its uncertainty, while our algorithm used their ratio for detecting the presence of aerosol in the upper troposphere.

To achieve this increase in the SNR of the LFA IF-USP lidar, a time average of 30 min and a vertical resolution of 375 m were found to be sufficient. Further studies are necessary to evaluate the occurrence of low clouds at this particular lidar site, and whether such a long time average is possible. Making changes to the system hardware, e.g., more powerful laser, filters with higher transmission, or PMTs with greater quantum efficiency, would be helpful. However, a detailed simulation of all optical components is necessary to evaluate the impact on the dynamic range of the system. Future studies are encouraged to investigate whether lidar systems in the visible or near-infrared, where molecular extinction is less significant, could be more suitable for detecting ultrafine particles. Another interesting consideration is whether the real vertical structure of the aerosol concentration in the upper troposphere, with alternating finer and thicker layers, could make a difference in the retrieval results.

Finally, although simulations and analysis were based on the LFA IF-USP lidar signal, in the presence of new organic particles formed in the Amazonian upper troposphere, our results are general and applicable to other instruments and sites.

Author Contributions: Conceptualization, H.M.J.B. and M.T.S.; methodology, validation and formal analysis, M.T.S.; investigation, M.T.S., J.L.G.-R., A.L.C. and D.A.G., H.M.J.B.; original draft preparation, M.T.S.; review and editing, M.T.S., J.L.G.-R., A.L.C., D.A.G. and H.M.J.B.; supervision, H.M.J.B. and J.L.G.-R. All authors have read and agreed to the published version of the manuscript.

Funding: M.T.S. and H.M.J.B. were funded by Conselho Nacional de Desenvolvimento Científico e Tecnológico (CNPq) grants number 132402/2020-3 and 308682/2017-3.

Data Availability Statement: Publicly available datasets were analyzed in this study. Data from the Manaus_EMBRAPA AERONET site can be found here: https://aeronet.gsfc.nasa.gov/cgi-bin/data_display_aod_v3?site=Manaus_EMBRAPA&nachal=2&level=1&place_code=10 (accessed on 28 July 2022). The HALO and G1 aircraft measurements of aerosol size and concentration were taken directly from [25]. For those interested in the actual data, it can be found here: <https://halo-db.pa.op.dlr.de/mission/5> (accessed on 28 July 2022), and here: <https://adc.arm.gov/discovery/#/results/s:aimms/iopShortName::aaf2014amazon> (accessed on 28 July 2022), respectively.

Acknowledgments: The authors gratefully acknowledge Bernhard Mayer, Claudia Emde, Josef Gasteiger and Arve Kylling for the provision of the LibRadtran radiative transfer model used in this publication. We also express our thanks for the technical support of Fernando Morais, Delano Campos, Glauber Cirino and Bruno Takeshi for maintaining and operating the lidar instrument used as a reference for the simulations performed in this study.

Conflicts of Interest: The authors declare no conflict of interest.

References

- Liou, K.N. Influence of Cirrus Clouds on Weather and Climate Processes: A Global Perspective. *Mon. Weather Rev.* **1986**, *114*, 1167–1199. [\[CrossRef\]](#)
- Betts, A.K.; Köhler, M.; Zhang, Y. Comparison of river basin hydrometeorology in ERA-Interim and ERA-40 reanalyses with observations. *J. Geophys. Res. Atmos.* **2009**, *114*. [\[CrossRef\]](#)
- Collow, A.B.M.; Miller, M.A. The Seasonal Cycle of the Radiation Budget and Cloud Radiative Effect in the Amazon Rain Forest of Brazil. *J. Clim.* **2016**, *29*, 7703–7722. [\[CrossRef\]](#)
- Saatchi, S.S.; Harris, N.L.; Brown, S.; Lefsky, M.; Mitchard, E.T.A.; Salas, W.; Zutta, B.R.; Buermann, W.; Lewis, S.L.; Hagen, S.; et al. Benchmark map of forest carbon stocks in tropical regions across three continents. *Proc. Natl. Acad. Sci. USA* **2011**, *108*, 9899–9904. [\[CrossRef\]](#) [\[PubMed\]](#)
- Zemp, D.C.; Schleussner, C.F.; Barbosa, H.M.J.; Van der Ent, R.J.; Donges, J.F.; Heinke, J.; Sampaio, G.; Rammig, A. On the importance of cascading moisture recycling in South America. *Atmos. Chem. Phys. Discuss.* **2014**, *14*, 17479–17526. [\[CrossRef\]](#)
- Marengo, J. On the hydrological cycle of the Amazon Basin: A historical review and current state-of-the-art. *Rev. Bras. Meteorol.* **2006**, *21*, 1–19.
- Arraut, J.M.; Nobre, C.; Barbosa, H.M.J.; Obregon, G.; Marengo, J. Aerial Rivers and Lakes: Looking at Large-Scale Moisture Transport and Its Relation to Amazonia and to Subtropical Rainfall in South America. *J. Clim.* **2012**, *25*, 543–556. [\[CrossRef\]](#)
- Davidson, E.A.; de Araújo, A.C.; Artaxo, P.; Balch, J.K.; Brown, I.F.; Bustamante, M.M.C.; Coe, M.T.; DeFries, R.S.; Keller, M.; Longo, M.; et al. The Amazon basin in transition. *Nature* **2012**, *481*, 321–328. [\[CrossRef\]](#)
- Fu, R.; Yin, L.; Li, W.; Arias, P.A.; Dickinson, R.E.; Huang, L.; Chakraborty, S.; Fernandes, K.; Liebmann, B.; Fisher, R.; et al. Increased dry-season length over southern Amazonia in recent decades and its implication for future climate projection. *Proc. Natl. Acad. Sci. USA* **2013**, *110*, 18110–18115. [\[CrossRef\]](#)
- Artaxo, P.; Rizzo, L.V.; Brito, J.F.; Barbosa, H.M.J.; Arana, A.; Sena, E.T.; Cirino, G.G.; Bastos, W.; Martin, S.T.; Andreae, M.O.; et al. Atmospheric aerosols in Amazonia and land use change: From natural biogenic to biomass burning conditions. *Faraday Discuss.* **2013**, *165*, 203. [\[CrossRef\]](#)
- Baars, H.; Ansmann, A.; Althausen, D.; Engelmann, R.; Heese, B.; Müller, D.; Artaxo, P.; Paixao, M.; Pauliquevis, T.; Souza, R. Aerosol profiling with lidar in the Amazon Basin during the wet and dry season. *J. Geophys. Res. Atmos.* **2012**, *117*. [\[CrossRef\]](#)
- Videla, F.C.; Barnaba, F.; Angelini, F.; Cremades, P.; Gobbi, G.P. The relative role of Amazonian and non-Amazonian fires in building up the aerosol optical depth in South America: A five year study (2005–2009). *Atmos. Res.* **2013**, *122*, 298–309. [\[CrossRef\]](#)
- Gatti, L.V.; Basso, L.S.; Miller, J.B.; Gloor, M.; Gatti Domingues, L.; Cassol, H.L.; Tejada, G.; Aragão, L.E.; Nobre, C.; Peters, W.; et al. Amazonia as a carbon source linked to deforestation and climate change. *Nature* **2021**, *595*, 388–393. [\[CrossRef\]](#) [\[PubMed\]](#)
- Ruiz-Vásquez, M.; Arias, P.A.; Martínez, J.A.; Espinoza, J.C. Effects of Amazon basin deforestation on regional atmospheric circulation and water vapor transport towards tropical South America. *Clim. Dyn.* **2020**, *54*, 4169–4189. [\[CrossRef\]](#)
- Agudelo, J.; Arias, P.A.; Vieira, S.C.; Martínez, J.A. Influence of longer dry seasons in the Southern Amazon on patterns of water vapor transport over northern South America and the Caribbean. *Clim. Dyn.* **2019**, *52*, 2647–2665. [\[CrossRef\]](#)
- Zemp, D.C.; Schleussner, C.F.; Barbosa, H.M.J.; Rammig, A. Deforestation effects on Amazon forest resilience. *Geophys. Res. Lett.* **2017**, *44*, 6182–6190. [\[CrossRef\]](#)
- Nobre, C.A.; Sellers, P.J.; Shukla, J. Amazonian Deforestation and Regional Climate Change. *J. Clim.* **1991**, *4*, 957–988. [\[CrossRef\]](#)

18. Laurance, W.F. Gaia's Lungs: Are rainforests inhaling Earth's excess carbon dioxide? *Nat. Hist.* **1999**, *108*, 96–96.
19. Correia, A.; Sena, E.; Dias, M.; Koren, I. Preconditioning, aerosols, and radiation control the temperature of glaciation in Amazonian clouds. *Commun. Earth Environ.* **2021**, *2*, 168. [\[CrossRef\]](#)
20. Gunthe, S.S.; King, S.M.; Rose, D.; Chen, Q.; Roldin, P.; Farmer, D.K.; Jimenez, J.L.; Artaxo, P.; Andreae, M.O.; Martin, S.T.; et al. Cloud condensation nuclei in pristine tropical rainforest air of Amazonia: Size-resolved measurements and modeling of atmospheric aerosol composition and CCN activity. *Atmos. Chem. Phys.* **2009**, *9*, 7551–7575. [\[CrossRef\]](#)
21. Franco, M.A.; Ditas, F.; Krempner, L.A.; Machado, L.A.T.; Andreae, M.O.; Araújo, A.; Barbosa, H.M.J.; de Brito, J.F.; Carbone, S.; Holanda, B.A.; et al. Occurrence and growth of sub-50 nm aerosol particles in the Amazonian boundary layer. *Atmos. Chem. Phys.* **2022**, *22*, 3469–3492. [\[CrossRef\]](#)
22. Andreae, M.O. The Aerosol Nucleation Puzzle. *Science* **2013**, *339*, 911–912. [\[CrossRef\]](#) [\[PubMed\]](#)
23. Varanda Rizzo, L.; Roldin, P.; Brito, J.; Backman, J.; Swietlicki, E.; Krejci, R.; Tunved, P.; Petäjä, T.; Kulmala, M.; Artaxo, P. Multi-year statistical and modeling analysis of submicrometer aerosol number size distributions at a rain forest site in Amazonia. *Atmos. Chem. Phys.* **2018**, *18*, 10255–10274. [\[CrossRef\]](#)
24. Wimmer, D.; Buenrostro Mazon, S.; Manninen, H.E.; Kangasluoma, J.; Franchin, A.; Nieminen, T.; Backman, J.; Wang, J.; Kuang, C.; Krejci, R.; et al. Ground-based observation of clusters and nucleation-mode particles in the Amazon. *Atmos. Chem. Phys.* **2018**, *18*, 13245–13264. [\[CrossRef\]](#)
25. Andreae, M.O.; Afchine, A.; Albrecht, R.; Holanda, B.A.; Artaxo, P.; Barbosa, H.M.J.; Borrmann, S.; Cecchini, M.A.; Costa, A.; Dollner, M.; et al. Aerosol characteristics and particle production in the upper troposphere over the Amazon Basin. *Atmos. Chem. Phys.* **2018**, *18*, 921–961. [\[CrossRef\]](#)
26. Wang, J.; Krejci, R.; Giangrande, S.; Kuang, C.; Barbosa, H.M.J.; Brito, J.; Carbone, S.; Chi, X.; Comstock, J.; Ditas, F.; et al. Amazon boundary layer aerosol concentration sustained by vertical transport during rainfall. *Nature* **2016**, *539*, 416–419. [\[CrossRef\]](#)
27. Kupc, A.; Williamson, C.J.; Hodshire, A.L.; Kazil, J.; Ray, E.; Bui, T.P.; Dollner, M.; Froyd, K.D.; McKain, K.; Rollins, A.; et al. The potential role of organics in new particle formation and initial growth in the remote tropical upper troposphere. *Atmos. Chem. Phys.* **2020**, *20*, 15037–15060. [\[CrossRef\]](#)
28. Martin, S.T.; Artaxo, P.; Machado, L.A.T.; Manzi, A.O.; Souza, R.A.F.; Schumacher, C.; Wang, J.; Andreae, M.O.; Barbosa, H.M.J.; Fan, J.; et al. Introduction: Observations and Modeling of the Green Ocean Amazon (GoAmazon2014/5). *Atmos. Chem. Phys.* **2016**, *16*, 4785–4797. [\[CrossRef\]](#)
29. Wendisch, M.; Pöschl, U.; Andreae, M.O.; Machado, L.A.T.; Albrecht, R.; Schlager, H.; Rosenfeld, D.; Martin, S.T.; Abdelmonem, A.; Afchine, A.; et al. ACRIDICON-CHUVA Campaign: Studying Tropical Deep Convective Clouds and Precipitation over Amazonia Using the New German Research Aircraft HALO. *Bull. Am. Meteorol. Soc.* **2016**, *97*, 1885–1908. [\[CrossRef\]](#)
30. Baars, H.; Ansmann, A.; Althausen, D.; Engelmann, R.; Artaxo, P.; Pauliquevis, T.; Souza, R. Further evidence for significant smoke transport from Africa to Amazonia. *Geophys. Res. Lett.* **2011**, *38*. [\[CrossRef\]](#)
31. Kulmala, M.; Asmi, A.; Lappalainen, H.K.; Baltensperger, U.; Brenguier, J.L.; Facchini, M.C.; Hansson, H.C.; Hov, Ø.; O'Dowd, C.D.; Pöschl, U.; et al. General overview: European Integrated project on Aerosol Cloud Climate and Air Quality interactions (EUCAARI); integrating aerosol research from nano to global scales. *Atmos. Chem. Phys.* **2011**, *11*, 13061–13143. [\[CrossRef\]](#)
32. Martin, S.T.; Andreae, M.O.; Althausen, D.; Artaxo, P.; Baars, H.; Borrmann, S.; Chen, Q.; Farmer, D.K.; Guenther, A.; Gunthe, S.S.; et al. An overview of the Amazonian Aerosol Characterization Experiment 2008 (AMAZE-08). *Atmos. Chem. Phys.* **2010**, *10*, 11415–11438. [\[CrossRef\]](#)
33. Marenco, F.; Johnson, B.; Langridge, J.M.; Mulcahy, J.; Benedetti, A.; Remy, S.; Jones, L.; Szpek, K.; Haywood, J.; Longo, K.; et al. On the vertical distribution of smoke in the Amazonian atmosphere during the dry season. *Atmos. Chem. Phys.* **2016**, *16*, 2155–2174. [\[CrossRef\]](#)
34. Barbosa, H.M.J.; Barja, B.; Pauliquevis, T.; Gouveia, D.A.; Artaxo, P.; Cirino, G.G.; Santos, R.M.N.; Oliveira, A.B. A permanent Raman lidar station in the Amazon: Description, characterization, and first results. *Atmos. Meas. Tech.* **2014**, *7*, 1745–1762. [\[CrossRef\]](#)
35. Holben, B.; Eck, T.; Slutsker, I.; Tanré, D.; Buis, J.; Setzer, A.; Vermote, E.; Reagan, J.; Kaufman, Y.; Nakajima, T.; et al. AERONET—A Federated Instrument Network and Data Archive for Aerosol Characterization. *Remote Sens. Environ.* **1998**, *66*, 1–16. [\[CrossRef\]](#)
36. Licel. *Licel PM-HV Photomultiplier Module R9880U—Manual*; Licel GmbH: Berlin, Germany, 2022. Available online: <https://licel.com/manuals/pmtmanual.pdf> (accessed on 28 July 2022).
37. Whiteman, D.N. Examination of the traditional Raman lidar technique. I. Evaluating the temperature-dependent lidar equations. *Appl. Opt.* **2003**, *42*, 2571–2592. [\[CrossRef\]](#)
38. Bucholtz, A. Rayleigh-scattering calculations for the terrestrial atmosphere. *Appl. Opt.* **1995**, *34*, 2765–2773. [\[CrossRef\]](#)
39. Bodhaine, B.A.; Wood, N.B.; Dutton, E.G.; Slusser, J. On Rayleigh Optical Depth Calculations. *J. Atmos. Ocean. Technol.* **1999**, *16*, 1854–1861. [\[CrossRef\]](#)
40. Anderson, G.; Clough, S.; Kneizys, F.; Chetwynd, J.; Shettle, E. *AFGL Atmospheric Constituent Profiles (0.120 km)*; Tech. Report AFGL-TR-0208, Environmental Research Papers, No. 954; Air Force Geophysics Laboratory, Hanscom AFB: Bedford, MA, USA, 1986. Available online: <https://apps.dtic.mil/sti/pdfs/ADA175173.pdf> (accessed on 28 July 2022).
41. Mayer, B.; Kylling, A. Technical note: The libRadtran software package for radiative transfer calculations—description and examples of use. *Atmos. Chem. Phys.* **2005**, *5*, 1855–1877. [\[CrossRef\]](#)

42. Holben, B.N.; Eck, T.F.; Slutsker, I.; Smirnov, A.; Sinyuk, A.; Schafer, J.; Giles, D.; Dubovik, O. Aeronet's Version 2.0 quality assurance criteria. In Proceedings of the SPIE Asia-Pacific Remote Sensing, Goa, India, 13–17 November 2006; Volume 6408, pp. 134–147. [[CrossRef](#)]
43. Klett, J.D. Lidar inversion with variable backscatter/extinction ratios. *Appl. Opt.* **1985**, *24*, 1638–1643. [[CrossRef](#)]
44. Fernald, F.G. Analysis of atmospheric lidar observations: Some comments. *Appl. Opt.* **1984**, *23*, 652–653. [[CrossRef](#)] [[PubMed](#)]
45. Gouveia, D.A.; Barja, B.; Barbosa, H.M.J.; Seifert, P.; Baars, H.; Pauliquevis, T.; Artaxo, P. Optical and geometrical properties of cirrus clouds in Amazonia derived from 1 year of ground-based lidar measurements. *Atmos. Chem. Phys.* **2017**, *17*, 3619–3636. [[CrossRef](#)]
46. Rocadenbosch, F.; Frasier, S.; Kumar, D.; Lange Vega, D.; Gregorio, E.; Sicard, M. Backscatter Error Bounds for the Elastic Lidar Two-Component Inversion Algorithm. *IEEE Trans. Geosci. Remote Sens.* **2012**, *50*, 4791–4803. [[CrossRef](#)]
47. Whiteman, D.N.; Demoz, B.; Rush, K.; Schwemmer, G.; Gentry, B.; Girolamo, P.D.; Comer, J.; Veselovskii, I.; Evans, K.; Melfi, S.H.; et al. Raman Lidar Measurements during the International H₂O Project. Part I: Instrumentation and Analysis Techniques. *J. Atmos. Ocean. Technol.* **2006**, *23*, 157–169. [[CrossRef](#)]
48. Torres, O.; Jethva, H.; Bhartia, P.K. Retrieval of Aerosol Optical Depth above Clouds from OMI Observations: Sensitivity Analysis and Case Studies. *J. Atmos. Sci.* **2012**, *69*, 1037–1053. [[CrossRef](#)]
49. Thorsen, T.J.; Ferrare, R.A.; Hostetler, C.A.; Vaughan, M.A.; Fu, Q. The impact of lidar detection sensitivity on assessing aerosol direct radiative effects. *Geophys. Res. Lett.* **2017**, *44*, 9059–9067. [[CrossRef](#)]
50. Winker, D.M.; Vaughan, M.A.; Omar, A.; Hu, Y.; Powell, K.A.; Liu, Z.; Hunt, W.H.; Young, S.A. Overview of the CALIPSO Mission and CALIOP Data Processing Algorithms. *J. Atmos. Ocean. Technol.* **2009**, *26*, 2310–2323. [[CrossRef](#)]
51. Winker, D.M.; Pelon, J.; Coakley, J.A.; Ackerman, S.A.; Charlson, R.J.; Colarco, P.R.; Flamant, P.; Fu, Q.; Hoff, R.M.; Kittaka, C.; et al. The CALIPSO Mission: A Global 3D View of Aerosols and Clouds. *Bull. Am. Meteorol. Soc.* **2010**, *91*, 1211–1230. [[CrossRef](#)]